






Third-order charge transport in a magnetic topological semimetal

Ziming Zhu ^{1,*} Huiying Liu ^{2,3,†} Yongheng Ge ¹ Zeying Zhang ³ Weikang Wu,³
Cong Xiao ^{4,5} and Shengyuan A. Yang ³

¹Key Laboratory of Low-Dimensional Quantum Structures and Quantum Control of Ministry of Education, Department of Physics and Synergetic Innovation Center for Quantum Effects and Applications, Hunan Normal University, Changsha 410081, China

²School of Physics, Beihang University, Beijing 100191, China

³Research Laboratory for Quantum Materials, Singapore University of Technology and Design, Singapore 487372, Singapore

⁴Department of Physics, The University of Hong Kong, Hong Kong, China

⁵HKU-UCAS Joint Institute of Theoretical and Computational Physics at Hong Kong, China



(Received 5 September 2022; revised 3 January 2023; accepted 26 April 2023; published 10 May 2023)

Magnetic topological materials and their physical signatures are a focus of current research. By first-principles calculations and symmetry analysis, we reveal exotic topological semimetal states in an existing antiferromagnet ThMn_2Si_2 . Depending on the Néel vector orientation, the topological band crossings near the Fermi level form either a double-nodal loop or two pairs of Dirac points, which are all fourfold degenerate and robust under spin-orbit coupling. These topological features produce large Berry connection polarizability, leading to pronounced nonlinear transport effects. Particularly, we evaluate the third-order current response, which dominates the transverse current in ThMn_2Si_2 . We show that the third-order response can be much more sensitive to topological phase transitions than a linear response, which offers a powerful tool for characterizing topological states of matter.

DOI: [10.1103/PhysRevB.107.205120](https://doi.org/10.1103/PhysRevB.107.205120)

I. INTRODUCTION

Topological semimetals (TSMs) have been attracting tremendous interest in the past decade [1–4]. They are characterized by protected band degeneracies near the Fermi level, which may form a variety of nodal points [5–11], nodal lines [12–14], or nodal surfaces [15–18] in momentum space. Due to these degeneracies, the low-energy electron excitations are endowed with exotic characters in dispersion, pseudospin structure, or topological charge, different from conventional materials.

Currently, despite exciting progress in the classifications of TSM states and in the high-throughput search of these materials [11,19–27], good candidate materials are still quite limited. Here, “good” means that the material should at least have a band degeneracy close to the Fermi level and not overlap with other extraneous bands. The challenge is more pronounced regarding the recent research focus of magnetic TSMs [28–31]. In many magnetic materials, the low-energy bands are quite complicated owing to the less dispersive d or f bands. In addition, many band degeneracies lose their protection under spin-orbit coupling (SOC), which is often sizable in magnetic materials.

In the meantime, there is an urgent need in exploring the physical consequences of TSM states. So far, experimental studies in the field are mainly in terms of spectroscopic probes, linear transport, and magnetotransport. We note that

band degeneracies can naturally give rise to strong interband coherence. For example, the Weyl points are singularities of Berry curvature [5], which is a band geometric quantity encoding interband coherence and scales as $\sim 1/(\Delta\varepsilon)^2$ in terms of the energy splitting $\Delta\varepsilon$ between two bands. Indeed, this underlies the large anomalous Hall response [32,33] and the chiral anomaly [34,35] effect proposed for Weyl semimetals. Following this thought, one naturally wonders whether there are other band geometric quantities enhanced in TSMs and what physical effects they may bring about.

In this paper, we first reveal a high-quality magnetic TSM in an existing antiferromagnetic (AFM) material ThMn_2Si_2 . We show that depending on its Néel vector direction, the band degeneracies can form a double-nodal loop or two pairs of Dirac points close to the Fermi level. These magnetic band crossings are fourfold degenerate and robust against SOC. Using this material as an example, we show that TSMs feature strongly enhanced Berry connection polarizability (BCP) [36–39], which is an intrinsic band geometric quantity and scales as $\sim 1/(\Delta\varepsilon)^3$. In ThMn_2Si_2 , it leads to a pronounced third-order charge current response to a driving E field, which dominates the transverse current. Furthermore, we show that the third-order signal is much more sensitive to the change in band topology than the linear order, so it offers a promising tool for characterizing TSMs.

II. ThMn_2Si_2 : STRUCTURE AND MAGNETISM

ThMn_2Si_2 single crystals were first synthesized in the 1960s [40,41]. They have a tetragonal CeAl_2Ge_2 -type structure with space group I_4/mmm (No. 139). As shown in

*zimingzhu@hunnu.edu.cn

†liuhuiying@pku.edu.cn

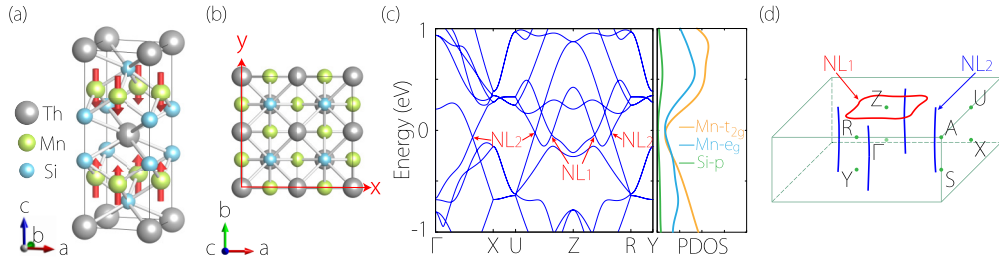


FIG. 1. (a) Perspective view and (b) top view of the ThMn₂Si₂ lattice. The magnetic structure in (a) represents the AFM-*z* state. (c) Band structure of ThMn₂Si₂ along with a projected density of states (PDOS) in the absence of SOC. The arrows mark the band crossing points belonging to two types of nodal lines, NL₁ and NL₂, as schematically illustrated in (d).

Figs. 1(a) and 1(b), the structure consists of atomic layers stacked along the *c* axis (*z* direction), with the Mn layer separated by Si-Th-Si sandwiches. Th atoms occupy the 2*a* Wyckoff position, whereas Mn (Si) atoms are at the position of 4*d* (4*e*). For the conventional cell in Fig. 1(a), the experimentally measured lattice constants are $a = b = 4.021 \text{ \AA}$ and $c = 10.493 \text{ \AA}$ [41]. These values are adopted in our first-principles calculations.

Experimental measurements showed that ThMn₂Si₂ is AFM with a Néel temperature $\sim 483 \text{ K}$ [42]. From the neutron diffraction result, the magnetism is mainly from Mn and has an A-type configuration, as illustrated in Fig. 1(a), i.e., the coupling is ferromagnetic within each Mn layer and is AFM between the layers. The magnetic easy axis is along *c*. The magnetic moment at Mn site was measured to be $\sim 1.75\mu_B$ at 78 K [42] and $< 2\mu_B$ at 4.2 K [43]. All these features have been successfully reproduced by our first-principles calculations (see Supplemental Material for details [44]).

III. NODAL LINES IN THE ABSENCE OF SOC

Let us first consider the band structure of AFM ThMn₂Si₂ in the absence of SOC. As shown in Fig. 1(c), the system exhibits a semimetal character. The low-energy bands around Fermi level are mainly from Mn-3*d* and Si-2*p* orbits. One observes multiple band crossings close to Fermi level [45]. A careful scan over the Brillouin zone (BZ) shows that they belong to two families of nodal lines, which form different winding patterns over the BZ torus [46]. As illustrated in Fig. 1(d), the first family (denoted as NL₁) consists of a single nodal ring located within the $k_z = \pi$ plane and centered at Z, whereas the second (denoted as NL₂) includes four nodal lines in the $k_x = 0$ and $k_y = 0$ planes, each traversing the BZ in the *z* direction.

To understand the protection of these nodal lines, we note that without SOC, the two spin channels are decoupled and hence can be analyzed separately. Each spin channel can be regarded as spinless and has an *effective* time-reversal symmetry T [47]. In addition, each channel has the symmetry of inversion (\mathcal{P}), vertical mirrors M_x and M_y , and horizontal glide mirror $\tilde{M}_z = \{M_z | \frac{1}{2}10\}$ (at a Mn layer). Therefore, the nodal lines actually enjoy a double protection. First, in each spin channel, the spinless \mathcal{PT} symmetry dictates a quantized π Berry phase on a small loop encircling a line, protecting it from opening a gap. Second, each line is protected by a mirror symmetry as the two crossing bands have opposite mirror

eigenvalues. The latter also constrains the nodal lines in the three mirror-invariant planes of BZ.

IV. DOUBLE-NODAL LOOP AND DIRAC POINTS UNDER SOC

Now, we study the band structure when SOC is included. We first consider the ground state with Néel vector along *z*, denoted as the AFM-*z* state. The system has a magnetic space group of $P14/nnc$. The calculated band structure in Fig. 2(a) looks similar to Fig. 1(c). Focusing on the band crossings in Fig. 2(a), one observes that the NL₂ lines are gapped out, however, surprisingly, the NL₁ ring is still maintained under SOC.

With SOC, each state $|u\rangle$ is degenerate with a partner $\mathcal{PT}|u\rangle$, where \mathcal{T} is the genuine time-reversal operation and \mathcal{P} here acts on the central Th site in Fig. 1(a). Hence, the NL₁ ring is fourfold degenerate, formed by crossing between two doubly \mathcal{PT} -degenerate bands. This is made possible if the \mathcal{PT} partners share the same \tilde{M}_z eigenvalue and the crossing is between bands with opposite eigenvalues, as illustrated in Fig. 2(b).

To verify this, note that

$$\tilde{M}_z^2 = -t_{110} = -e^{-ik_x - ik_y}, \quad (1)$$

with t_{110} the translation of one lattice unit respectively in the *x* and *y* directions, so its eigenvalues are given by $g_z = \pm ie^{-i(k_x + k_y)/2}$. Due to the offset between the inversion center (Th site) and the mirror plane (Mn layer), the commutation relation between \mathcal{P} and \tilde{M}_z is $\tilde{M}_z\mathcal{P} = t_{111}\mathcal{P}\tilde{M}_z$. It follows that

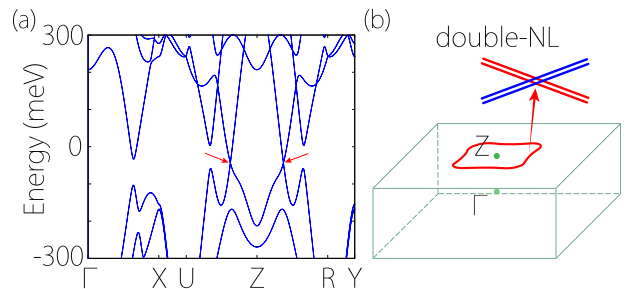


FIG. 2. (a) Band structure with SOC for the AFM-*z* state. The arrows indicate the crossing points on the double-nodal loop, as illustrated in (b). Each point on the loop is formed by the crossing of four bands. The red and blue colors denote bands with opposite \tilde{M}_z eigenvalues.

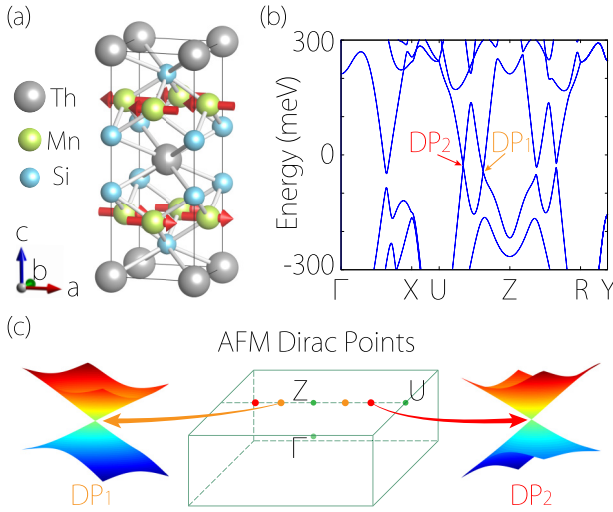


FIG. 3. (a) Magnetic structure for the AFM- x state. (b) shows the corresponding band structure with SOC. The arrows mark two (of the four) Dirac points on the Z - U path. (c) illustrates the distribution and the dispersion of these Dirac points.

for any state $|u\rangle$ with $\tilde{M}_z|u\rangle = g_z|u\rangle$, its partner satisfies

$$\tilde{M}_z(\mathcal{PT}|u\rangle) = -e^{-ik_z}g_z(\mathcal{PT}|u\rangle). \quad (2)$$

Thus, in the $k_z = \pi$ plane, the \mathcal{PT} partners indeed share the same eigenvalue g_z .

This kind of fourfold nodal loop robust under SOC was initially proposed by Fang *et al.* [14] and was named the double-nodal loop. Its material realizations are very rare, especially in magnetic systems, being only predicted in MnPd_2 up to now [30].

A key feature of magnetic TSMs is that their topological states can be controlled by rotating the magnetic order parameter, e.g., by spin torques, applied field, or strain, which changes the symmetry of the system. Here, let us consider the case when the Néel vector is along the x direction (referred to as the AFM- x state), as in Fig. 3(a). This breaks the fourfold rotation along z and the magnetic space group becomes $P_1m_1m_1$. As shown in Fig. 3(b), points on the NL_1 and NL_2 nodal lines are almost all gapped out except for four points, namely the intersection points of these lines with the Z - U path [Fig. 3(c)]. These points represent fourfold-degenerate AFM Dirac points. Hence, when the Néel vector rotates from the z to x direction, the system transitions from a magnetic double-nodal loop semimetal to an AFM Dirac semimetal.

To understand this topological phase transition, we note that (1) the \mathcal{PT} symmetry is maintained regardless of the Néel vector direction, (2) \tilde{M}_z is broken for AFM- x , so the double-nodal loop is no longer protected, and (3) there emerges a twofold screw axis $\tilde{C}_{2x} = \{C_{2x}|\frac{1}{2}0\}$. This \tilde{C}_{2x} symmetry, together with \mathcal{PT} , protects the four Dirac points on the \tilde{C}_{2x} -invariant path Z - U . The analysis is similar to that for the AFM- z case and hence is relegated to the Supplemental Material [44].

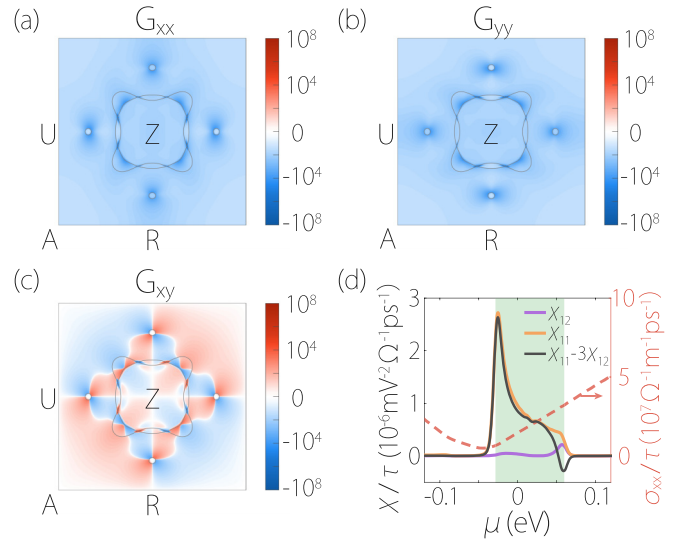


FIG. 4. (a)–(c) Calculated distribution of BCP tensor elements in the $k_z = \pi$ plane for the AFM- z state. The gray lines depict the Fermi surface. The unit of G_{ab} is $\text{\AA}^2 \text{V}^{-1}$. (d) Third-order conductivity tensor elements (divided by τ) vs the chemical potential μ for AFM- z . Here, we also plot the longitudinal conductivity σ_{xx} (red dashed line, right axis). The energy range of the double-nodal loop is indicated by the green shaded region.

V. BCP AND THIRD-ORDER CURRENT RESPONSE

As the Berry curvature, BCP is an intrinsic band geometric quantity, which characterizes the positional shift of Bloch electrons under an applied E field [36–39]. It is a second-rank tensor. For a band with index n , it can be expressed as (we set $e = \hbar = 1$) [36]

$$G_{ab}(\mathbf{k}) = 2 \text{Re} \sum_{m \neq n} \frac{(v_a)_{nm}(v_b)_{mn}}{(\varepsilon_n - \varepsilon_m)^3}, \quad (3)$$

where a and b label the Cartesian components, v 's are the interband velocity matrix elements, and ε_n is the band energy. From (3), one can see that $\text{BCP} \sim 1/(\Delta\varepsilon)^3$, so it should be strongly enhanced at small gap regions, especially at band degeneracies. In Figs. 4(a)–4(c), we plot BCP components for the AFM- z state in the $k_z = \pi$ plane where the double-nodal loop is located. One clearly observes that BCP is concentrated around the nodal loop as well as the four small-gap spots where the original NL_2 lines cross the plane.

In TSMs, band degeneracies exist near the Fermi level, which means pronounced BCP would appear for the low-energy states, thereby impacting the physical properties of the system. Recently, it was revealed that BCP underlies many nonlinear response properties of solids [38,39,48–51]. Here, we consider the third-order charge current response. This is because ThMn_2Si_2 has a quite high symmetry: It has the symmetry $\mathcal{T}t_{00\frac{1}{2}}$, \mathcal{P} , and also C_{4z} in the ground state AFM- z . Notably, the inversion symmetry \mathcal{P} forbids any second-order current response, whether it is intrinsic from BCP [49,50] or extrinsic from the Berry curvature dipole [52,53]. Considering transport in the x - y plane, these symmetries suppress both the linear- and second-order current responses in the direction

transverse to E . Thus, the third-order current $j \sim E^3$ will be the leading-order transverse response.

In the extended semiclassical theory, BCP determines the third-order current that is linear in the electron relaxation time τ [39]. The corresponding third-order conductivity tensor can be expressed as [39]

$$\chi_{abcd} = \tau \left[\int [dk] (-\partial_a \partial_b G_{cd} + \partial_a \partial_d G_{bc} - \partial_b \partial_d G_{ac}) f_0 + \frac{1}{2} \int [dk] v_a v_b G_{cd} f_0'' \right], \quad (4)$$

where $[dk]$ stands for $\sum_n dk/(2\pi)^d$ with d the dimension of the system, the v 's here are the intraband velocity for the band n , and f_0 is the Fermi distribution function. Considering in-plane transport, the indices $a, b, c, d \in \{x, y\}$. Obviously, the χ tensor is most easily evaluated in a coordinate system adapted to the crystal, as in Fig. 1(b). The direction of applied E field can be specified by its polar angle θ , i.e., $\mathbf{E} = E(\cos \theta, \sin \theta, 0)$. Note that expression (4) includes both the longitudinal and transverse responses. Focusing on the transverse third-order current $j_{\perp}^{(3)}$ which is along $\hat{z} \times \mathbf{E}$, we can write $j_{\perp}^{(3)} = \chi_{\perp}(\theta) E^3$ in terms of a third-order transverse conductivity χ_{\perp} . For the ground-state ThMn_2Si_2 with C_{4z} symmetry, we find

$$\chi_{\perp}(\theta) = -\frac{1}{4}(\chi_{11} - 3\chi_{12}) \sin 4\theta, \quad (5)$$

where $\chi_{11} = \chi_{xxxx}$, and $\chi_{12} = (\chi_{xyxy} + \chi_{yxyx} + \chi_{yyxx})/3$.

In Fig. 4(d), we plot the involved tensor elements for ThMn_2Si_2 as a function of chemical potential. One observes that the response is peaked around the intrinsic Fermi level, in a window overlapping with the energy range of the double-nodal loop (the green shaded region). This indicates that the contribution is mainly due to the double-nodal loop and confirms our claim that band degeneracies in TSMs tend to enhance BCP and generate pronounced third-order transport.

VI. PROBING TOPOLOGICAL PHASE TRANSITION

We have shown that the third-order response is greatly enhanced by band degeneracies in TSMs. As a result, when there is a change in the degeneracy, i.e., when the system undergoes a topological phase transition, a significant change in the nonlinear response can be expected.

Here, we demonstrate this point in ThMn_2Si_2 . When the Néel vector direction rotates from z to x , a topological phase transition happens, with the double-nodal loop replaced by four Dirac points. Note that for the AFM- x state, the C_{4z} symmetry is broken, so there are more independent elements of χ , and the expression for χ_{\perp} changes to

$$\chi_{\perp}(\theta) = (3\chi_{21} - \chi_{11}) \cos^3 \theta \sin \theta + (\chi_{22} - 3\chi_{12}) \cos \theta \sin^3 \theta, \quad (6)$$

where $\chi_{22} = \chi_{yyyy}$, and $\chi_{21} = (\chi_{yyxx} + \chi_{yxyx} + \chi_{xyyx})/3$. Figure 5(a) plots the relevant tensor elements versus chemical potential. Compared with Fig. 4(d), one can see a dramatic change in the response. The contribution from the original nodal loop is largely suppressed. Instead, the two peaks in Fig. 5(a) are perfectly aligned with the energies of the two

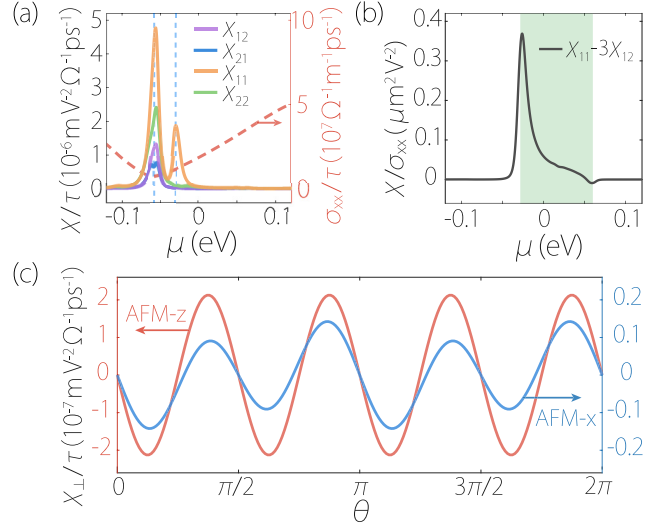


FIG. 5. (a) Third-order conductivity tensor elements (divided by τ) vs μ for the AFM- x state. The two vertical dashed lines mark the energies of the AFM Dirac points. The corresponding longitudinal conductivity σ_{xx} is also shown by the red dashed curve. (b) The ratio $(\chi_{11} - 3\chi_{12})/\sigma_{xx}$ plotted vs μ for AFM- z state. (c) Comparison of $\chi_{\perp}(\theta)$ (divided by τ) for AFM- z (red line) and AFM- x (blue line). The AFM- z result is an order of magnitude larger than AFM- x , and they show different angular dependence.

pairs of Dirac points (as marked by the two vertical dashed lines).

In Fig. 5(c), we plot $\chi_{\perp}(\theta)$ at the intrinsic Fermi level for the two states, as a function of angle θ . One can see that the response for AFM- x is smaller than AFM- z by an order of magnitude, despite the overall similarity of the two band structures [see Figs. 2(a) and 3(b)]. For comparison, in Figs. 4(d) and 5(a), we also plot the linear Drude conductivity for each state (red dashed curve), which shows much less change between the two states. This demonstrates that the third-order response from BCP is indeed much more sensitive to the change in band topology, thereby offering a promising tool for probing topological phase transitions.

In addition, from Fig. 5(c), one notes that the third-order response $\chi_{\perp}(\theta)$ exhibits different angular dependence for the two states. For AFM- z , $\chi_{\perp}(\theta)$ has a period of $\pi/2$, whereas the period is doubled for AFM- x . This feature can be tested in experiment using a multiple-lead geometry [48,54].

VII. DISCUSSION

We have revealed ThMn_2Si_2 as an almost ideal magnetic TSM hosting two exotic topological states. Its magnetism persists at room temperature, and its band structure is clean with degeneracies close to the Fermi level (energy spread of the nodal loop is also quite small). By controlling the Néel vector direction, the system realizes a magnetic double-nodal loop semimetal or a AFM Dirac semimetal.

These topological band features can be probed by angle-resolved photoemission spectroscopy (ARPES) [4]. However, it is often difficult for ARPES to clearly resolve tiny gaps

such as those appearing during topological phase transitions. In such cases, the BCP-enhanced third-order current response can be a good complement to existing characterization techniques. Experimentally, the nonlinear signal is typically detected using the lock-in technique with a low-frequency ac driving field, which was successfully applied in several recent experiments [48,54–56].

The double-nodal loop TSM can be a parent state for generating multiple topological states under symmetry breaking. Besides AFM Dirac semimetals, other states, such as Weyl semimetals or magnetic topological insulators, may also appear by controlling magnetic ordering, lattice strain, or external fields. The third-order current response will be useful in characterizing such transitions.

The third-order conductivity χ_{\perp} studied here is connected with BCP, which is peaked at band degeneracies. In good TSMs, this peak occurs near the intrinsic Fermi level, as shown in Fig. 4(d). Meanwhile, the linear conductivity σ typically reaches a minimum at the same range, because as a semimetal the density of states is suppressed there, as

confirmed in Figs. 4(d) and 5(a). This contrasting behavior again manifests the important geometric origin of nonlinear transport. In Fig. 5(b), we further plot the ratio χ/σ versus the chemical potential, which is even more enhanced at topological band degeneracies. It may serve as an intrinsic material property (free of τ) that can be compared among different materials.

ACKNOWLEDGMENTS

The authors thank D. L. Deng for valuable discussions. This work is supported by the Project of Educational Commission of Hunan Province of China (Grant No. 21A0066), the Hunan Provincial Natural Science Foundation of China (Grant No. 2022JJ30370), the National Natural Science Foundation of China (Grant No. 11704117), the UGC/RGC of Hong Kong SAR (AoE/P-701/20), and the Singapore NRF CRP22-2019-0061. We acknowledge computational support from H2 clusters in Xi'an Jiaotong University and the National Supercomputing Centre Singapore.

-
- [1] C. K. Chiu, J. C. Y. Teo, A. P. Schnyder, and S. Ryu, *Rev. Mod. Phys.* **88**, 035005 (2016).
- [2] B. Yan and C. Felser, *Annu. Rev. Condens. Matter Phys.* **8**, 337 (2017).
- [3] N. P. Armitage, E. J. Mele, and A. Vishwanath, *Rev. Mod. Phys.* **90**, 015001 (2018).
- [4] B. Q. Lv, T. Qian, and H. Ding, *Rev. Mod. Phys.* **93**, 025002 (2021).
- [5] X. Wan, A. M. Turner, A. Vishwanath, and S. Y. Savrasov, *Phys. Rev. B* **83**, 205101 (2011).
- [6] S. Murakami, *New J. Phys.* **9**, 356 (2007).
- [7] S. M. Young, S. Zaheer, J. C. Y. Teo, C. L. Kane, E. J. Mele, and A. M. Rappe, *Phys. Rev. Lett.* **108**, 140405 (2012).
- [8] C. Fang, M. J. Gilbert, X. Dai, and B. A. Bernevig, *Phys. Rev. Lett.* **108**, 266802 (2012).
- [9] B.-J. Yang and N. Nagaosa, *Nat. Commun.* **5**, 4898 (2014).
- [10] B. Bradlyn, J. Cano, Z. Wang, M. Vergniory, C. Felser, R. J. Cava, and B. A. Bernevig, *Science* **353**, aaf5037 (2016).
- [11] Z. M. Yu, Z. Zhang, G. B. Liu, W. K. Wu, X. P. Li, R. W. Zhang, S. A. Yang, and Y. G. Yao, *Sci. Bull.* **67**, 375 (2022).
- [12] S. A. Yang, H. Pan, and F. Zhang, *Phys. Rev. Lett.* **113**, 046401 (2014).
- [13] H. Weng, Y. Liang, Q. Xu, R. Yu, Z. Fang, X. Dai, and Y. Kawazoe, *Phys. Rev. B* **92**, 045108 (2015).
- [14] C. Fang, H. Weng, X. Dai, and Z. Fang, *Chin. Phys. B* **25**, 117106 (2016).
- [15] Q. F. Liang, J. Zhou, R. Yu, Z. Wang, and H. Weng, *Phys. Rev. B* **93**, 085427 (2016).
- [16] C. Zhong, Y. Chen, Y. Xie, S. A. Yang, M. L. Cohen, and S. Zhang, *Nanoscale* **8**, 7232 (2016).
- [17] T. Bzdusek and M. Sgrist, *Phys. Rev. B* **96**, 155105 (2017).
- [18] W. K. Wu, Y. Liu, S. Li, C. Y. Zhong, Z. M. Yu, X. L. Sheng, Y. X. Zhao, and S. A. Yang, *Phys. Rev. B* **97**, 115125 (2018).
- [19] F. Tang, H. C. Po, A. Vishwanath, and X. Wan, *Nat. Phys.* **15**, 470 (2019).
- [20] T. Zhang, Y. Jiang, Z. Song, H. Huang, Y. He, Z. Fang, H. Weng, and C. Fang, *Nature (London)* **566**, 475 (2019).
- [21] F. Tang, H. C. Po, A. Vishwanath, and X. Wan, *Nature (London)* **566**, 486 (2019).
- [22] M. Vergniory, L. Elcoro, C. Felser, N. Regnault, B. A. Bernevig, and Z. Wang, *Nature (London)* **566**, 480 (2019).
- [23] Y. Xu, L. Elcoro, Z. D. Song, B. J. Wieder, M. Vergniory, N. Regnault, Y. Chen, C. Felser, and B. A. Bernevig, *Nature (London)* **586**, 702 (2020).
- [24] Y. Jiang, Z. Fang, and C. Fang, *Chin. Phys. Lett.* **38**, 077104 (2021).
- [25] F. Tang and X. Wan, *Phys. Rev. B* **104**, 085137 (2021).
- [26] G. B. Liu, Z. Zhang, Z. M. Yu, S. A. Yang, and Y. Yao, *Phys. Rev. B* **105**, 085117 (2022).
- [27] Z. Zhang, G. B. Liu, Z. M. Yu, S. A. Yang, and Y. Yao, *Phys. Rev. B* **105**, 104426 (2022).
- [28] P. Tang, Q. Zhou, G. Xu, and S. C. Zhang, *Nat. Phys.* **12**, 1100 (2016).
- [29] G. Hua, S. Nie, Z. Song, R. Yu, G. Xu, and K. Yao, *Phys. Rev. B* **98**, 201116(R) (2018).
- [30] D. F. Shao, G. Gurung, S. H. Zhang, and E. Y. Tsymlal, *Phys. Rev. Lett.* **122**, 077203 (2019).
- [31] Y. Jin, X. T. Zeng, X. Feng, X. Du, W. Wu, X.-L. Sheng, Z. M. Yu, Z. Zhu, and S. A. Yang, *Phys. Rev. B* **104**, 165424 (2021).
- [32] K. Y. Yang, Y. M. Lu, and Y. Ran, *Phys. Rev. B* **84**, 075129 (2011).
- [33] A. A. Burkov, *Phys. Rev. Lett.* **113**, 187202 (2014).
- [34] A. Vilenkin, *Phys. Rev. D* **22**, 3080 (1980).
- [35] D. T. Son and B. Z. Spivak, *Phys. Rev. B* **88**, 104412 (2013).
- [36] Y. Gao, S. A. Yang, and Q. Niu, *Phys. Rev. Lett.* **112**, 166601 (2014).
- [37] Y. Gao, S. A. Yang, and Q. Niu, *Phys. Rev. B* **91**, 214405 (2015).
- [38] Y. Gao, *Front. Phys.* **14**, 33404 (2019).
- [39] H. Y. Liu, J. Z. Zhao, Y. X. Huang, X. L. Feng, C. Xiao, W. K. Wu, S. Lai, W. B. Gao, and S. A. Yang, *Phys. Rev. B* **105**, 045118 (2022).
- [40] M. Sikirica and Z. Ban, *Croat. Chem. Acta* **36**, 151 (1964).
- [41] Z. Ban and M. Sikirica, *Acta Crystallogr.* **18**, 594 (1965).

- [42] Z. Ban, L. Omejec, A. Szytuła, and Z. Tomkowicz, *Phys. Status Solidi A* **27**, 333 (1975).
- [43] K. S. V. L. Narasimhan, V. U. S. Rao, W. E. Wallace, and I. Pop, *AIP Conference Proceedings* **29**, 594 (1976).
- [44] See Supplemental Material at <http://link.aps.org/supplemental/10.1103/PhysRevB.107.205120> for details of the computational method, band structure by the modified Becke-Johnson potential, a symmetry analysis for AFM Dirac points, a low-energy effective model for Dirac points, an energy comparison for different magnetic configurations, and about the correlation effect for the Th-6d orbit, which includes Refs. [42,43,57–63].
- [45] Here, if counting spin, each band is doubly degenerate, and the crossing is fourfold degenerate.
- [46] S. Li, Z. M. Yu, Y. Liu, S. Guan, S. S. Wang, X. Zhang, Y. Yao, and S. A. Yang, *Phys. Rev. B* **96**, 081106(R) (2017).
- [47] D. Vanderbilt, *Berry Phases in Electronic Structure Theory: Electric Polarization, Orbital Magnetization and Topological Insulators* (Cambridge University Press, Cambridge, UK, 2018).
- [48] S. Lai, H. Liu, Z. Zhang, J. Zhao, X. Feng, N. Wang, C. Tang, Y. Liu, K. Novoselov, S. A. Yang *et al.*, *Nat. Nanotechnol.* **16**, 869 (2021).
- [49] C. Wang, Y. Gao, and D. Xiao, *Phys. Rev. Lett.* **127**, 277201 (2021).
- [50] H. Liu, J. Zhao, Y. X. Huang, W. Wu, X. L. Sheng, C. Xiao, and S. A. Yang, *Phys. Rev. Lett.* **127**, 277202 (2021).
- [51] C. Xiao, H. Liu, W. Wu, H. Wang, Q. Niu, and S. A. Yang, *Phys. Rev. Lett.* **129**, 086602 (2022).
- [52] I. Sodemann and L. Fu, *Phys. Rev. Lett.* **115**, 216806 (2015).
- [53] J. I. Facio, D. Efremov, K. Koepf, J.-S. You, I. Sodemann, and J. van den Brink, *Phys. Rev. Lett.* **121**, 246403 (2018).
- [54] K. Kang, T. Li, E. Sohn, J. Shan, and K. Mak, *Nat. Mater.* **18**, 324 (2019).
- [55] Q. Ma, S. Y. Xu, H. Shen, D. MacNeill, V. Fatemi, T. R. Chang, A. M. Mier Valdivia, S. Wu, Z. Du, C. H. Hsu *et al.*, *Nature (London)* **565**, 337 (2019).
- [56] C. Wang, R. C. Xiao, H. Liu, Z. Zhang, S. Lai, C. Zhu, H. Cai, N. Wang, S. Chen, Y. Deng *et al.*, *Nat. Sci. Rev.* **9**, nwac020 (2022).
- [57] P. E. Blöchl, *Phys. Rev. B* **50**, 17953 (1994).
- [58] G. Kresse and J. Furthmüller, *Phys. Rev. B* **54**, 11169 (1996).
- [59] G. Kresse and D. Joubert, *Phys. Rev. B* **59**, 1758 (1999).
- [60] J. P. Perdew, K. Burke, and M. Ernzerhof, *Phys. Rev. Lett.* **77**, 3865 (1996).
- [61] S. L. Dudarev, G. A. Botton, S. Y. Savrasov, C. J. Humphreys, and A. P. Sutton, *Phys. Rev. B* **57**, 1505 (1998).
- [62] F. Tran and P. Blaha, *Phys. Rev. Lett.* **102**, 226401 (2009).
- [63] A. A. Mostofi, J. R. Yates, Y.-S. Lee, I. Souza, D. Vanderbilt, and N. Marzari, *Comput. Phys. Commun.* **178**, 685 (2008).